Quantitative Modeling of the Equilibration of Two-Phase Solid-Liquid Fe by Atomistic Simulations on Diffusive Time Scales

Ebrahim Asadi

Mohsen Asle Zaeem
Missouri University of Science and Technology, zaeem@mst.edu

Sasan Nouranian

Michael I. Baskes

Recommended Citation

Quantitative modeling of the equilibration of two-phase solid-liquid Fe by atomistic simulations on diffusive time scales

Ebrahim Asadi,[1,*] Mohsen Asle Zaeem,[1,*] Sasan Nouranian,[2] and Michael I. Baskes[3]

[1]*Department of Materials Science and Engineering, Missouri University of Science and Technology, Rolla, Missouri 65409, USA*
[2]*Department of Chemical Engineering, The University of Mississippi, University, Mississippi 38677, USA*
[3]*Department of Aerospace Engineering, Mississippi State University, Mississippi State, Mississippi 39762, USA*

In this paper, molecular dynamics (MD) simulations based on the modified-embedded atom method (MEAM) and a phase-field crystal (PFC) model are utilized to quantitatively investigate the solid-liquid properties of Fe. A set of second nearest-neighbor MEAM parameters for high-temperature applications are developed for Fe, and the solid-liquid coexisting approach is utilized in MD simulations to accurately calculate the melting point, expansion in melting, latent heat, and solid-liquid interface free energy, and surface anisotropy. The required input properties to determine the PFC model parameters, such as liquid structure factor and fluctuations of atoms in the solid, are also calculated from MD simulations. The PFC parameters are calculated utilizing an iterative procedure from the inputs of MD simulations. The solid-liquid interface free energy and surface anisotropy are calculated using the PFC simulations. Very good agreement is observed between the results of our calculations from MEAM-MD and PFC simulations and the available modeling and experimental results in the literature. As an application of the developed model, the grain boundary free energy of Fe is calculated using the PFC model and the results are compared against experiments.

I. INTRODUCTION

The phase-field crystal (PFC) model utilizes a constant density in the liquid and a periodic density in the solid, which provide atomistic scale details applicable to diffusive time scales [1,2]. Utilizing the PFC approach in the modeling of different phenomena in materials science has increased significantly over the past couple of years [3–14], because many properties such as elasticity, plasticity, and grain boundary energies are naturally incorporated in the model. Since PFC is directly derived from classical density functional theory (CDFT) [15], it is also an effective model to quantitatively simulate grain growth in materials, and to determine materials properties such as elastic constants and the solid-liquid interface free energy. The simplest form for the solid-liquid free energy in the PFC model is [1,2,16,17]

$$F = \int_V \left\{ \frac{1}{2}\phi(\mathbf{r})\left[\alpha + \lambda\left(q_0^2 + \nabla^2\right)^2\right]\phi(\mathbf{r}) + \frac{g}{4}\phi(\mathbf{r})^4 \right\} d\mathbf{r},$$

where $\phi(\mathbf{r})$ is a function related to the density field and α, λ, q_0, and g are the model parameters. Indeed, the critical task in quantitative modeling of a solid-liquid system using PFC is determining the model parameters. Wu and Karma [18] suggested a set of relations based on the Ginzburg-Landau (GL) theory and a multiscale analysis to determine the PFC parameters for body-centered-cubic (bcc)-liquid structures (GL-PFC relations). In GL-PFC, assuming that $\varepsilon = -\alpha/\lambda q_0^4$ is small, the parameters α, λ, and q_0 are related to the location and height of the first peak of the liquid structure factor at the melting point and its second derivative. The GL-PFC also utilizes the average solid and liquid densities

and the fluctuation amplitude of atoms in the solid state to obtain the parameter g. Good agreement between the solid-liquid interface free energy of Fe predicted by GL-PFC and available results from molecular dynamics (MD) simulations was reported by Wu and Karma [18]. Jaatinen *et al.* [19] used a common tangent between solid and liquid densities to update the parameters of the nonlinear parts of PFC, which resulted in minor improvements over the calculations of GL-PFC. They also introduced an eighth-order fitting PFC (EOF-PFC), which significantly improves the prediction of the expansion in melting by the PFC model. However, EOF-PFC increases the computational time considerably, because the order of spatial derivative in the free energy of the system increases from four to eight. The EOF-PFC was also used to quantitatively calculate the grain boundary free energy of Fe at the melting point, in qualitative agreement with the experiments. Kapikranian *et al.* [20] also calculated the grain boundary free energy of Fe in dimensionless unit using a PFC model based on atomic density function.

The PFC input parameters (melting point, liquid structure factor, and fluctuation amplitude in the solid) can be determined from experiments or computational methods such as MD simulations. Measuring the input parameters for PFC by experiment is a challenging task because the measurements should be done at the melting point [21]. On the other hand, MD simulations can be used to obtain these input parameters at a lower cost [22]. For instance, Wu and Karma [18] and Jaatinen *et al.* [19] both utilized the results of MD simulations based on an embedded atom method (EAM) potential for Fe [23] and that provided by Sun *et al.* [24]. Therefore, providing accurate input parameters from MD simulations is another important factor in the quantitative modeling of the equilibration of the two-phase solid-liquid structure by PFC. In addition, other properties such as the solid-liquid interface free energy and surface anisotropy can be determined from MD simulations for comparison with the PFC predictions.

---

*Corresponding authors: AsadiE@mst.edu; Zaeem@mst.edu

Determining the exact melting point in MD simulations is of crucial importance because it is required for constructing the equilibrated solid-liquid structures. It is also known that the melting point calculated by MD simulations may vary significantly depending on the interatomic potential used. Sun *et al.* [24] utilized different potentials in MD simulations to simulate the solid-liquid equilibrium structure of Fe. They calculated properties such as melting point, latent heat, expansion in melting, and solid-liquid interface free energy and surface anisotropy. In particular, they calculated the melting point (experiment: 1811 K), latent heat (experiment: 13.8 kJ/mol), and expansion in melting (experiment: $0.38 - 0.45$ Å^3/atom) of Fe to be 1772 K, 15.6 kJ/mol, and 0.62 Å^3/atom, respectively, using EAM Mendelev, Han, Srolovitz, Ackland, Sun, and Asta [MH(SA)^2] [23] potentials. Watanabe *et al.* [25] recently used the Finnis-Sinclair [26] potential with parameters developed by Ackland and Finnis [27] to calculate the same properties for Fe and found a much higher melting point (2400 K) than the experiments. Liu *et al.* [28,29] recently tested a number of potentials for the calculations of solid-liquid interface properties using MD simulations. They showed that the EAM potential presented by Ackland *et al.* [30] predicts a closer melting point (1791 K) to the experiments. However, their calculations do not improve the prediction of the latent heat (16.0 kJ/mol). The modified EAM (MEAM) potential developed by Jelinek *et al.* [31] was recently employed by Asadi *et al.* [32] to investigate the melting properties of Fe. These calculations resulted in a melting point prediction of 1931.3 K, a latent heat prediction of 13.7 kJ/mol, and an expansion in melting prediction of 0.55 Å^3/atom. While utilizing the MEAM parameter set in MD simulations has improved the prediction of the latent heat and the expansion in melting significantly, it has failed to predict the melting point accurately. This is because the MEAM potential used by Asadi *et al.* [32] was originally developed for Fe-Al-Mg-Cu-Si binary alloy systems. It is worth mentioning that the MEAM potentials of a single element have never been utilized to simulate the equilibration of two-phase solid-liquid Fe for accurate calculation of the interface properties.

In this paper, we present quantitative modeling and simulations of the solid-liquid equilibration for Fe on atomistic and diffusive time scales by MD and PFC simulations, respectively. This paper is organized in two major sections: Sec. II, which deals with the MEAM-MD simulations of equilibrating solid-liquid structure of Fe and providing the input properties for the PFC model, and Sec. III, which contains an iterative approach for determining the model parameters of PFC and simulating the equilibration of the two-phase solid-liquid structure of Fe on diffusive time scales.

In Sec. II, a second nearest-neighbor (2NN) MEAM parameter set for Fe is presented for applications near the melting point, which is utilized in all the MD simulations presented here. The solid-liquid coexistence approach [24] is utilized to calculate the melting point, expansion in melting, and latent heat. Then, an order parameter in the concept of the capillary fluctuation method (CFM) is defined to identify atoms as liquid or solid during the simulations, and the solid-liquid interface free energy and surface anisotropy of

Fe are determined. These properties are compared with their available counterparts in the literature to verify the accuracy of the current calculations. Finally, the liquid structure factor and atoms fluctuations are determined from MD simulations as the input properties for the PFC model. Where it is appropriate, the simulations are repeated in different crystallographic directions with a different number of atoms to verify that the calculations are size- and orientation-independent.

In Sec. III, a PFC model is employed to simulate the equilibration of the two-phase solid-liquid structure of Fe on a diffusive time scale. First, an iterative procedure is developed to determine the PFC parameters based on the input properties calculated in Sec. II. Then, the sixth-order governing equation of the PFC model is converted to three second-order partial differential equations (PDEs), and this system of equations are solved numerically using the finite element method (FEM). A convergence study is conducted on the element and model sizes to make sure that the results are mesh- and size-independent. The expansion in melting, solid-liquid interface free energy, and surface anisotropy are calculated using PFC simulations and compared with the MEAM-MD results and the available counterparts from the literature. Furthermore, a comparison between the computing time for MD and PFC models to simulate the solid-liquid equilibrium structure is also presented. Finally, as an example of the capabilities of the quantitative PFC model, the grain boundary free energy of Fe near the melting point is calculated and compared to the experimental results.

II. MD SIMULATIONS

In this section, the development of a set of 2NN-MEAM parameters for high-temperature applications of Fe is presented. This parameter set is adopted in MD simulations to investigate solid-liquid properties. First, the exact melting point of Fe is calculated using the coexistence approach, and then the latent heat, expansion in melting, and solid-liquid interface free energy, and surface anisotropy are determined and compared to the available results in the literature to test the accuracy of the calculations. Furthermore, the liquid structure factor and fluctuations of atoms in the solid state at the melting point are calculated as the input properties to determine the PFC model parameters in Sec. III. Unless otherwise mentioned, the parallel MD code LAMMPS [33] with the time step size of 0.002 ps is used for all the MD simulations, and the boundary conditions are periodic in all directions.

A. Modified-embedded atom method

Modified-embedded atom method (MEAM) [34] is a semiempirical many-body interatomic potential for metals, metallic alloys, metal hydrides, carbides, and nitrides. It is widely used in the atomistic and MD simulations of unary, binary, ternary, and multicomponent metallic systems encompassing a variety of microstructural features, such as free surfaces, grain boundaries, and defects. Recently, MEAM was parameterized for saturated hydrocarbons [35], extending its applicability further to the molecular simulations of organics and hybrid organic/metallic material systems.

TABLE I. 2NN MEAM parameters for Fe. E^0 (eV) is the cohesive energy; R^0 (Å) is the nearest-neighbor distance in the equilibrium reference structure; α^0 is the exponential decay factor for the universal equation of state (UEOS) of Rose *et al.* [41]; A is the electron density scaling factor for the embedding function; δ^a and δ^r are the attraction ($a^* > 0$) and repulsion ($a^* \leqslant 0$) cubic terms for the universal equation of state; $\beta^{(0-3)}$ are the exponential decay factors for the atomic electron densities; $t^{(1-3)}$ are the weighting parameters for the atomic electron densities; and $C_{\min}$ and $C_{\max}$ are the screening parameters for three atoms of iron.

E^0	R^0	α^0	A	δ^a	δ^r	$\beta^{(0)}$	$\beta^{(1)}$	$\beta^{(2)}$	$\beta^{(3)}$	$t^{(1)}$	$t^{(2)}$	$t^{(3)}$	$C_{\min}$	$C_{\max}$
4.29	**2.47**[a]	**5.03**[a]	0.57	0.00	0.00	3.67	1.00	1.00	1.00	2.90	1.00	**−8.7**[a]	0.16	2.80

[a]Original values from Lee and Baskes [37] are: 2.48, 5.07, and −8.5, respectively.

In the MEAM formalism [34–36], the total energy of a single-element system is given by

$$E_{\text{tot}} = \sum_i \left[F_i(\bar{\rho}_i) + \frac{1}{2} \sum_{j(\neq i)} S_{ij} \phi_{ij}(R_{ij}) \right], \quad (1)$$

where F_i is the "embedding energy" function (energy required to embed an atom in the background electron density $\bar{\rho}_i$ at site i), S_{ij} is the screening factor between atoms at sites i and j, and ϕ_{ij} is the pair interaction between atoms at sites i and j with a separation distance of R_{ij}. We do not intend to present the full MEAM formalism in this paper; interested readers are directed to Refs. [34,35,37,38] on the details of MEAM theory. We focus on introducing the MEAM parameters (Table I) and their effect on different terms of the total energy of the MEAM [Eq. (1)], especially parameters A, $t^{(1)}$, and $t^{(3)}$, which have the most significant effect on the melting point of the element (discussed in Sec. II B).

The embedding function in Eq. (1) is given by

$$F_i(\bar{\rho}_i) = \begin{cases} AE^0 \frac{\bar{\rho}_i}{\bar{\rho}_i^0} \left(\ln \frac{\bar{\rho}_i}{\bar{\rho}_i^0} \right) & \text{if } \bar{\rho}_i \geqslant 0, \\ -AE^0 \frac{\bar{\rho}_i}{\bar{\rho}_i^0} & \text{if } \bar{\rho}_i < 0, \end{cases} \quad (2)$$

where A is an arbitrary scaling factor, E^0 is the cohesive energy, and $\bar{\rho}_i^0$ is the background electron density for the atom at site i in its reference (typically equilibrium) structure. The background electron density is

$$(\bar{\rho}_i)^2 = \sum_{l=0}^{3} t^{(l)} (\rho^{(l)})^2, \quad (3)$$

where $t^{(h)}$ ($h = 1, 2,$ and 3) are adjustable parameters, $\rho_i^{(0)}$ is the spherically symmetric partial electron density, and $\rho_i^{(1)}$, $\rho_i^{(2)}$, and $\rho_i^{(3)}$ are angular partial electron densities related to the three-body cos, $\cos^2$, and $\cos^3$ dependence of the background electron density [39], respectively. Furthermore, the expressions for the partial electron densities include atomic electron densities $\rho^{a(h)}$ ($h = 0, 1, 2,$ and 3), which in turn use $\beta^{(h)}$($h = 0, 1, 2,$ and 3) as another set of adjustable element-dependent parameters.

The screening factor S_{ij} is defined as $S_{ij} = \prod_{k \neq i,j} S_{ikj}$, where the interaction between atoms at sites i and j are screened by neighboring atoms at the site k, which $S_{ij} = 1$ means that the interaction between atoms at sites i and j is not screened and $S_{ij} = 0$ that the interaction is completely screened. The screening factor S_{ijk} includes parameters $C_{\min}$ and $C_{\max}$ to determine the extent of screening of atoms at sites i and j by an atom at site k.

The rest of the parameters at Table I ($R^0, \alpha^0, \delta^a,$ and δ^r) are utilized in the definition of the pair interaction function ϕ_{ij}, which can be calculated using the first NN (1NN) [34] or the 2NN [40] formalism.

B. 2NN MEAM parameters for iron

In this paper, we used the 2NN parameters for Fe published by Lee and Baskes [37] as the starting point and modified them slightly to better fit the physical properties of Fe at high temperatures; i.e., we included the experimental melting point in the fitting procedure. Since the main objective of this paper has been to perform high-temperature simulations of Fe, we utilized the coexistence approach to calculate the melting point more accurately (see Sec. II B). The original parameters in the Lee and Baskes paper [37] predict a melting temperature of 1837 K using the coexistence approach, which is actually closer to the experimental value of 1811 K than the value of 1900–2100 K, reported in the abovementioned reference [37]. The modified set of 2NN MEAM parameters for Fe are summarized in Table I. In this table, the modified parameters are in bold, and their values are compared to the original values reported by Lee and Baskes. For all calculations and simulations, a cutoff value of 4.0 Å was used. The properties of Fe, as predicted by MEAM, are compared to the experimental data in Table II. The values of these properties are very similar to those presented in the Lee and Baskes paper [37] except for the melting point.

The parameters A, $t^{(1)}$, and $t^{(3)}$ have the most significant effect on the melting point of Fe. The parameter A is the scaling factor of the embedding function at Eq. (2). The parameters $t^{(1)}$ and $t^{(3)}$ are the coefficients of cos and $\cos^3$ dependent partial electron densities. Therefore, it can be inferred that the amount of the asymmetric background electron density mostly controls the melting point in the MEAM potential. Among the parameters mentioned above, we only modified the $t^{(3)}$ parameter to better reproduce the melting point of Fe (Table II) and kept the original values of the A and $t^{(1)}$ parameters. At the same time, we modified the parameter r_e and α^0 (Table I) to give the correct reproduction of the other physical properties of Fe in Table II with respect to the experimental values (the complete experimental data for Fe can be found in Ref. [42]).

C. Melting point

It is well known that the melting point (T_M) of a material calculated by MD simulations depends on the interatomic potentials [29] used in the MD simulations. Therefore, the first step in investigating the equilibration of a solid-liquid structure by MD simulations is to accurately determine the melting

TABLE II. 2NN MEAM-MD simulation results versus experimental data [37] of physical properties of Fe. B (10^{12} dyn/cm^2) is the bulk modulus; C_{11}, C_{12}, and C_{44} (10^{12} dyn/cm^2) are elastic constants; $E_{(100)}$, $E_{(110)}$, and $E_{(111)}$ (erg/cm^2) are surface energies in the (100), (110), and (111) planes, respectively; E_v^f (eV) is the relaxed vacancy formation energy; ΔE's (eV/atom) are structural energy differences; ΔR (Å) is the relative change in the nearest-neighbor distance; ε (10^{-6}/K) is the coefficient of linear thermal expansion; C_P (J/mol K) is the specific heat; and MP (K) is the melting point.

Property	2NN MEAM-MD	Exp. (Ref. [37])
B	1.66	1.67
C_{11}	2.31	2.30
C_{12}	1.34	1.35
C_{44}	1.16	1.17
$E_{(100)}$	2526	–
$E_{(110)}$	2369	2360
$E_{(111)}$	2685	–
E_v^f	1.59	1.6-2.0
$\Delta E_{bcc \rightarrow fcc}$	0.044	0.082
$\Delta E_{fcc \rightarrow hcp}$	−0.015	−0.023
$\Delta R_{bcc \rightarrow fcc}$	0.080	0.064
ε (0–100 °C)	11.18	12.10
C_P (0–100 °C)	26.18	25.50
MP	1807	1811

point. A simulation box consisting of $m \times n \times l$ periodic solid cells are initially used to calculate the accurate melting point; the l direction, which is normal to the solid-liquid interface, is longer than the other two directions. In order to construct a solid-liquid coexisting structure, the whole simulation box is initially equilibrated as solid at an estimated guess of the melting point. A method to determine an estimated guess of the melting point is explained in detail by Asadi *et al.* [32]. After the equilibration, the central half of the simulation box is melted at a high temperature, while the other half is held fixed in a canonical ensemble (*NVT*) using Nosé-Hoover thermostating [43,44]. Then, the melted half of the simulation box is equilibrated at the estimated guess of the melting point using an isothermal-isobaric ensemble (*NPT*) for 0.5 ns, while its associated box size in the normal direction is allowed to relax and the other half (solid) is still fixed. Next, the entire simulation box is allowed to relax in the normal direction for 1 ns using an *NPT* ensemble at the estimated guess of the melting point to minimize the pressure in all directions. Finally, the refined value of the melting point is calculated using an isenthalpic ensemble (*NPH*) lasting for a long time (∼10 ns), while the size of the box in the normal direction can relax to minimize the normal pressure. The whole process is repeated using the calculated refined temperature as the new estimate for the melting point until the calculated melting point is converged. Table III shows the calculated melting point versus different simulation box sizes and three different normal directions. The calculated melting point is converged for a simulation box consisting of ∼100,000 atoms. There is a slight variation of the melting point depending on the orientation of the simulation box [45], which is much less than the variation of the melting point caused by changing the number of atoms in the simulation box. Therefore, if a large

TABLE III. The calculated melting point versus the size and the orientation of the MD simulation box.

Orientation	Size	Atoms	T_M (K)
$[001] \times [010] \times [001]$	$8 \times 8 \times 96$	12288	1809.6
$[001] \times [010] \times [001]$	$12 \times 12 \times 144$	41472	1807.9
$[001] \times [010] \times [001]$	$16 \times 16 \times 192$	98304	1807.2
$[001] \times [1\bar{1}0] \times [110]$	$15 \times 11 \times 132$	81720	1806.7
$[1\bar{1}0] \times [11\bar{2}] \times [111]$	$11 \times 7 \times 108$	99792	1807.8

enough simulation box is chosen, it can be concluded that the calculated melting point is size and orientation independent. The melting point for the developed MEAM parameters is determined to be the average value of the melting point for the three orientations, i.e., $T_M = 1807$ K.

Table IV compares the calculated melting point (T_M), latent heat (L), and expansion in melting (ΔV) with the experimental data and the results of some other MD simulations. Utilizing the current MEAM parameters in MD simulations results in calculating the melting point of Fe very close to the experiment, which is more accurate compared with all the other MD simulation results. The best prediction of MD simulations for the expansion in melting (6% error compared to experiments) is also achieved by simulations using the current MEAM parameters. There are two other MEAM-MD simulation results listed in Table IV predicting the latent heat slightly closer to the experiment than the current simulations. However, both of them reported significantly higher melting points, and one of them calculated significantly higher expansion in melting. It is worth mentioning that we have performed simulations to investigate the effect of the increment of the melting point on the latent heat. We observed that the latent heat increases by ∼2% for a 100 K increment of the melting point. Considering this fact, our prediction of the latent heat is still reasonable compared to the MEAM calculations by Lee *et al.* [40], and it is in the order of the MEAM calculations of Asadi *et al.* [32].

D. Solid-liquid interface free energy

Consider a snapshot of an equilibrating solid-liquid slab of Fe with two Cartesian coordinate systems denoted by unit vectors: (a) $\hat{z}_1, \hat{z}_2$, and $\hat{z}_3$, parallel to the [100], [010], and [001] directions, respectively, and (b) $\hat{x}_1, \hat{x}_2$, and $\hat{x}_3$, parallel to the periodic directions of the simulation box, denoted by $[a_1 b_1 c_1]$, $[a_2 b_2 c_2]$, and $[a_3 b_3 c_3]$, respectively. For brevity, we also use x, y, and z to refer to the width, thickness, and normal directions of the slab, respectively. Without loss of generality, the explained solid-liquid coexisting structure is depicted in Fig. 1, where $[a_1 b_1 c_1] = [001]$, $[a_2 b_2 c_2] = [1\bar{1}0]$, and $[a_3 b_3 c_3] = [110]$. In Fig. 1, the atoms are colored based on the value of the order parameters (ψ), which will be defined later in this section. The order parameter can be used to identify an atom as liquid or solid, and the color of the atoms in Fig. 1 changes from red (liquid) to blue (solid) at the solid-liquid interface. Thus, the solid-liquid interface, $h(x)$, can be identified based on the values of the order parameter. The solid-liquid interface can be assumed unaffected in the $\hat{x}_2$ direction for $b \ll W$; therefore, the unit vector normal to

TABLE IV. Comparison of the calculated melting point (T_M), latent heat (L), and expansion in melting (ΔV) with other MD simulations and experiments.

Method	T_M (K)	(%) [a]	L (kJ/mol)	(%)	ΔV (Å^3/atom)	(%)
EAM[b]	1791	1.1%	16.0	16%		
EAM: MH (SA)[c]	1772	2.2%	15.6	13%	0.62	49%
MEAM[d]	1900–2000	7.7%	13.2	4.4%		
MEAM[e]	1931.3	6.6%	13.7	0.7%	0.55	33%
Exp. Data[f]	1811		13.8		0.38–0.45	
MEAM; present paper	1807	0.2%	13.0	5.8%	0.44	6.0%

[a]The error percent over experiments; the quantity is averaged for the data with two values.
[b]References [29,30]
[c]References [23,24]
[d]References [40,46]
[e]References [31,32]
[f]References [23,24,47]

the interface, $\hat{n} = n_1\hat{z}_1 + n_2\hat{z}_2 + n_3\hat{z}_3$, is only a function of the interface position in the $\hat{x}_1$ direction and can be shown in terms of the angle between $\hat{x}_1$ and the interface plane, θ, as

$$n_i = (\sin\theta \, \hat{x}_1 + \cos\theta \, \hat{x}_3) \cdot \hat{z}_i, \qquad (4)$$

where $i = 1,2,3$, and the relationship between the two sets of the unit vectors is $\hat{x}_i = (a_i\hat{z}_1 + b_i\hat{z}_2 + c_i\hat{z}_3)/\sqrt{a_i^2 + b_i^2 + c_i^2}$. The solid-liquid interface free energy [$\gamma(\hat{n})$] can be approximated in terms of its anisotropy using a finite number of spherical harmonics with cubic symmetry [48]. For weakly anisotropic crystals, using the first three spherical harmonics results in a reasonable approximation for the interface free energy [49,50], yielding:

$$\gamma(\hat{n})/\gamma_0 = 1 + \delta_1 \left(\sum_{i=1}^{3} n_i^4 - 3/5 \right)$$
$$+ \delta_2 \left(3\sum_{i=1}^{3} n_i^4 + 66n_1^2 n_2^2 n_3^2 - 17/7 \right), \quad (5)$$
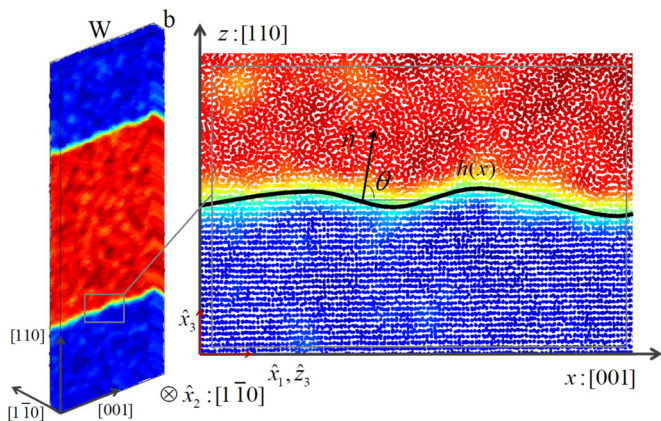
where δ_1 and δ_2 are anisotropies and γ_0 is the average interface free energy. The relationship between $\gamma(\hat{n})$ and θ can be obtained by substituting Eq. (4) into Eq. (5) for different orientations of the interface plane. Since the interfacial stiffness, $(\gamma + d^2\gamma/d\theta^2)|_{\theta=0}$, is more anisotropic than γ by an order of magnitude, it is more convenient to utilize its definition for determining the anisotropies. In theory, we only need to calculate the interface stiffness for three orientations to find γ_0, δ_1, and δ_2. However, we calculate the interface stiffness for five orientations for validation purposes. The expressions for interface stiffness are shown in Table V. For instance, the orientation $\langle 100 \rangle \{001\}$ means that $\hat{x}_1$ is parallel to the $\langle 100 \rangle$ direction and the solid-liquid interface plane is $\{001\}$.

Another expression for the interface stiffness can be derived by calculating the amount of energy required to alter the solid-liquid interface from its averaged value. The Fourier expansion of the solid-liquid interface is $h(x) = \sum_{k=0}^{\infty} A(k)\exp(ikx) +$ c.c., where c.c. refers to the related complex conjugate terms. Following the energy equilibration, the mean energy of each Fourier mode should be constant and equal to $k_B T_M$ [51]; therefore, the interface energy relation becomes $k_B T_M = b\int\gamma(\theta)ds$, where $ds = \sqrt{1 + (dh/dx)^2}$. Using the approximations $\theta \approx dh(x)/dx$ and $\sqrt{1 + (dh/dx)^2} \approx 1 + \theta^2/2$, the desired relation for the interface stiffness is obtained as

$$\gamma + d^2\gamma/d\theta^2 = \frac{k_B T_M}{bW\langle|A(k)|^2\rangle k^2}, \qquad (6)$$

where $\langle|A(k)|^2\rangle$ is the mean-square amplitude of the Fourier modes for the solid-liquid interface. Thus, the interface stiffness can be calculated from the slope of the line fitted to $k_B T_M/bW\langle|A(k)|^2\rangle$ and k^2 data, which is also equal to the relations in the second column of Table V for the given orientation. Consequently, the problem of calculating the solid-liquid interface free energy and surface anisotropy is reduced to the determination of the solid-liquid interface and its Fourier transform for different orientations for which MD simulations will be utilized.

In order to determine $h(x)$, the solid-liquid coexisting simulation box, which was explained in the preceding section, is used for the simulations. The simulation box consists of

FIG. 1. (Color online) Snapshot of the solid-liquid coexisting structure for the $\langle 001 \rangle \{110\}$ orientation. The atoms are colored based on their order parameters (ψ), and the color of atoms changes from red (liquid) to blue (solid) at the solid-liquid interface.

TABLE V. The solid-liquid interface stiffness ($\gamma + d^2\gamma/d\theta^2$) calculated analytically using Eq. (5) and by MEAM-MD simulations. The 95% confidence intervals for the MEAM-MD calculated stiffness are shown in the parentheses.

Orientation	Size (Å)	Expression (Eq. 5)	MEAM-MD (mJ/m^2)
$\langle 100 \rangle \{001\}$	$233.6 \times 11.7 \times 624.4$	$\gamma_0[1 - (18/5)\delta_1 - (80/7)\delta_2]$	159.4(13)
$\langle 1\bar{1}0 \rangle \{110\}$	$247.8 \times 11.7 \times 717.0$	$\gamma_0[1 + (39/10)\delta_1 + (155/14)\delta_2]$	219.5(14)
$\langle 001 \rangle \{110\}$	$233.6 \times 12.4 \times 714.7$	$\gamma_0[1 - (21/10)\delta_1 + (365/14)\delta_2]$	152.3(6)
$\langle 1\bar{1}0 \rangle \{111\}$	$247.8 \times 14.3 \times 723.9$	$\gamma_0[1 + (12/5)\delta_1 - (1280/63)\delta_2]$	221.8(17)
$\langle 11\bar{2} \rangle \{111\}$	$250.3 \times 12.4 \times 645.6$	$\gamma_0[1 + (12/5)\delta_1 - (1280/63)\delta_2]$	215.6(12)

$m \times n \times l$ periodic cells, and the equilibrating temperature for the simulation box is $T_M = 1807\ K$. Since, the simulation box is equilibrated at the exact melting point of the MEAM parameters, the final *NPH* thermostating is taken to be only 240 ps, and a snapshot of the atoms' positions is taken every 0.2 ps (total of 1201 frames). For each snapshot, the order parameter used by Sun *et al.* [24] Here $\phi = (1/14) = \sum |\vec{r}_i - \vec{r}_{\text{bcc}}|^2$ is calculated where the summation is over eight 1NNs and six 2NNs, and $\vec{r}_{\text{bcc}}$ is the neighbors' positions in the perfect bcc lattice. As mentioned earlier [50], this definition of the order parameter results in oscillations of ϕ, which makes the identification of the interface location challenging. Therefore, we utilize a new order parameter for each atom as

$$\psi = \frac{\sum_i w_d\, r_i\, \phi_i}{\sum_i w_d\, r_i}, \qquad (7)$$

where $w_d = [1 - (\frac{r_i}{d})^2]^2$, $r_i = \sqrt{(x_i - x)^2 + (z_i - z)^2}$, d is the radius of the smoothing cylinder for ψ, and the summation is over the atoms in the smoothing distance $r_i < d$. It is worth mentioning that the definition in Eq. (7) results in a continuous function of the order parameter with damped oscillations for a sufficiently big smoothing radius. Figure 2 compares ϕ and ψ at a location in the x direction, where ϕ is averaged over a cubic bin of the L_{bcc} size, $d = 2.5 L_{\text{bcc}}$, and L_{bcc} is the lattice parameter of Fe at $T_M = 1807$ K. The value of the order parameters are typically small at solid (~ 0.13) and bigger at liquid (~ 0.28). At the interface location, the order parameter

changes from ~ 0.13 to ~ 0.28; therefore, the interface location is identified as the location where the order parameter takes its average value at the solid and liquid ($\psi_{\text{int}} = 0.20$).

Once $h(x)$ is known, the Fourier transform is applied to calculate the fluctuation amplitudes of each frame, and the amplitudes are averaged over all the frames and both interfaces in the structure (total of 2402 data sets) to find $\langle |A(k)|^2 \rangle$. The variation of $k_B T_M / bW \langle |A(k)|^2 \rangle$ versus k^2 is shown in Fig. 3 for four different orientations; the data for the $\langle 1\bar{1}0 \rangle \{111\}$ orientation is not shown because the results are very similar to the results of the $\langle 11\bar{2} \rangle \{111\}$ orientation. A 95% confidence line is fitted for the data of each orientation using the least-square method, where the slope of the line equals to the interface stiffness. It was observed that $k_B T_M / bW \langle |A(k)|^2 \rangle$ does not fall on the fitted line for very big and small k values. This might be because of the numerical round off errors for larger values of k, where the values of the fluctuation amplitudes are too small. Thus, we use a finite number of modes in our fitting such that the norm of the residuals is less than three. The length of the k^2 axis at (Fig. 3) where the data fall on the fitted line was not less than 0.11 (the biggest value was 0.2 related to the $\langle 001 \rangle \{110\}$ orientation) for all the orientations and is in the same order of the data provided in other papers using the capillary fluctuation method (CFM) method to calculate the interface stiffness [24,29]. We have also performed a convergence study to verify that our stiffness calculations are independent of smoothing distance
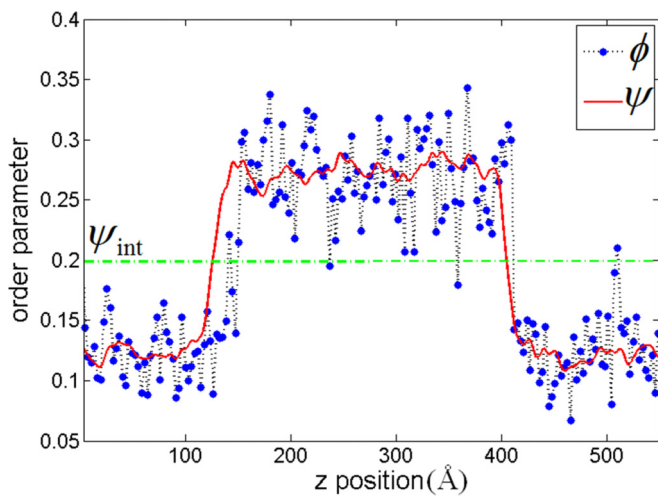

FIG. 2. (Color online) Plot of the order parameters ϕ (Sun *et al.* [24]) and ψ (this paper) versus the z direction for a box with $80 \times 4 \times 210$ periodic cells at the $\langle 100 \rangle \{001\}$ orientation.
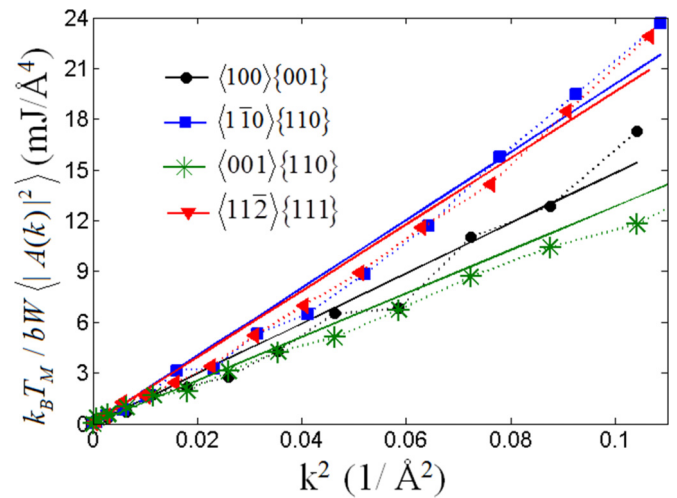

FIG. 3. (Color online) Plot of $k_B T_M / bW \langle |A(k)|^2 \rangle$ versus k^2 of Fe at 1807 K for three different orientations. The solid lines represent the 95% confidence line for each orientation.

TABLE VI. Solid-liquid interface free energy and surface anisotropy parameters of Fe calculated by MD simulations using different interatomic potentials. The 95% confidence intervals are shown in the parentheses.

Potential	$\gamma_0 (mJ/m^2)$	δ_1 (%)	δ_2 (%)
EAM: ABCH[a]	206(10)	1.6(0.12)	−0.04(0.28)
EAM: MH(SA)[b]	175(11)	3.3(0.18)	0.24(0.32)
Pair[c]	221(14)	1.3(0.18)	0.26(0.28)
EAM[d]	184(5)	3.5(0.85)	0.1(0.14)
MEAM; present paper	188(14)	5.2(0.07)	−0.31(0.11)

[a]References [24,52].
[b]References [23,24].
[c]References [24,53].
[d]Reference [29].

and thickness of the slab. All the stiffness calculations are converged for a smoothing distance as big as $d/L_{bcc} = 2.5$ and simulation box sizes reported in Table V. It is worth mentioning that utilizing a small b makes equilibrating solid-liquid structure challenging, and utilizing a very big b results in changing the behavior of the $1/\langle|A(k)|^2\rangle - k^2$ curve from linear to logarithmic.

The converged solid-liquid interface stiffness along with the 95% confidence intervals (in parentheses) for each orientation, which is calculated from the slope of the fitted lines in Fig. 3, is reported in Table V. We utilized the expressions for the $\langle 100 \rangle\{001\}$, $\langle 1\bar{1}0 \rangle\{110\}$, and $\langle 001 \rangle\{110\}$ orientations in Table V to calculate γ_0, δ_1, and δ_2. The calculated results are reported in Table VI. The interface stiffness of the other two orientations ($\langle 1\bar{1}0 \rangle\{111\}$ and $\langle 11\bar{2} \rangle\{111\}$) are determined by substituting the calculated γ_0, δ_1, and δ_2 parameters for each element into the related stiffness expressions (the two expressions are the same, and the calculated value is 223.1). These results are compared with the MEAM-MD calculations (the last two rows in Table V); the maximum difference for this comparison is around 3%. This difference is roughly the norm of the residuals used in the line fitting when calculating the stiffness. Therefore, the use of Eq. (6) to estimate the solid-liquid interface free energy is an appropriate method to express its anisotropy (with about 3% error).

The interface free energy and surface anisotropy parameters calculated by using other MD methods are also listed in Table VI. The calculated interface free energy is in a fair agreement with the results of other MD methods. MEAM predicts negative δ_2 surface anisotropy parameter, which was only seen for the EAM Ackland, Bacon, Calder, Harry (ABCH) potential [52]. It should also be noted that the anisotropy parameters δ_1 and δ_2 correspond to the fourfold and sixfold symmetries, respectively, and the negative sign of δ_2 is in more agreement with the PFC results, which will be discussed more in Sec. III C.

E. Structure factor

The PFC model parameters in Sec. III will be determined based on the liquid structure factor and the fluctuations of atoms in the solid state, both calculated at the melting point. In this subsection, MD simulations are employed to

determine the liquid structure factor. The liquid structure factor is calculated by applying Fourier transform to the radial distribution function, $g(r)$, of the liquid state as

$$S(k) = 1 + 4\pi \rho_l \int_0^R r^2 [g(r) - 1]$$
$$\times \frac{\sin(kr)}{kr} \frac{\sin(\pi r/R)}{\pi r/R} dr, \quad k < k_{min},$$

$$S(k) = 1 + 4\pi \rho_l \int_0^R r^2 [g(r) - 1]$$
$$\times \frac{\sin(kr)}{kr} dr, \quad k > k_{min}, \quad (8)$$

where R is half of the size of the simulation box, and the window function $\sin(\pi r/R)/(\pi r/R)$ is introduced to avoid the fluctuations of the structure factor at small wavelengths [54]. However, using the window function for all of the ks tends to decrease the values of the peaks in the structure factors, especially the value of the first peak. Therefore, the window function will be used to calculate $S(k)$ for $k < k_{min}$, where k_{min} is a value smaller than the location of the first peak.

To calculate $g(r)$ at the liquid regions, a simulation box consisting of $20 \times 20 \times 20$ lattice cells was melted and equilibrated for 0.5 ns at $T_M = 1807$ K with zero pressure in all directions. Then, $g(r)$ was calculated and averaged over 0.5 ns. In order to reduce the amount of fluctuations of the structure factor at small waves and to improve the accuracy of the calculations, it is necessary to calculate $g(r)$ for a distance up to 20.0 Å, which is larger than the force cutoff distance (4.0 Å) for MEAM parameters. This was done by postprocessing the positions of atoms obtained from MD simulations and not by changing the force cutoff of the MEAM potential. Figure 4 shows $g(r)$ for Fe from our simulations and two experimental measurements.

By substituting the calculated radial distribution function into Eq. (8) and determining the resultant integral numerically for different k values, the liquid structure factor of Fe is calcu-
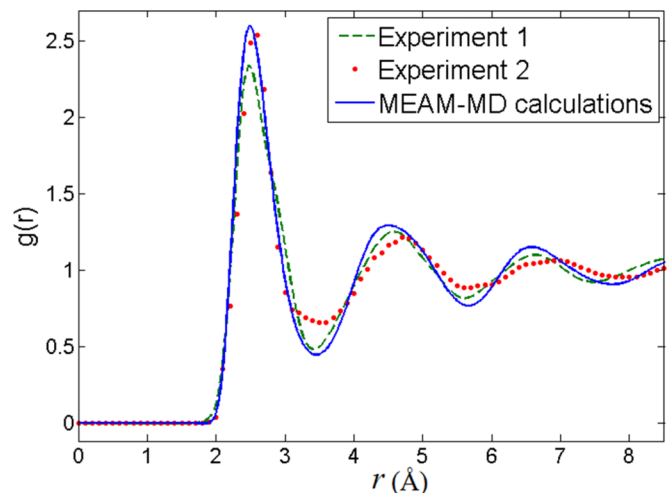

FIG. 4. (Color online) Radial distribution function, $g(r)$, for Fe calculated by MEAM-MD simulations at 1807 K, Experiment 1 performed by Il'inskii *et al.* [55] at 1820 K and presented in Mendelev *et al.* [23], and Experiment 2 performed by Waseda [56] at 1833.15 K.

FIG. 5. (Color online) Liquid structure factor, $S(k)$, for Fe calculated by MEAM-MD simulations at 1807 K, Experiment 1 performed by Il'inskii *et al.* [55] at 1820 K and presented in Mendelev *et al.* [23], and Experiment 2 performed by Waseda [56] at 1833.15 K.
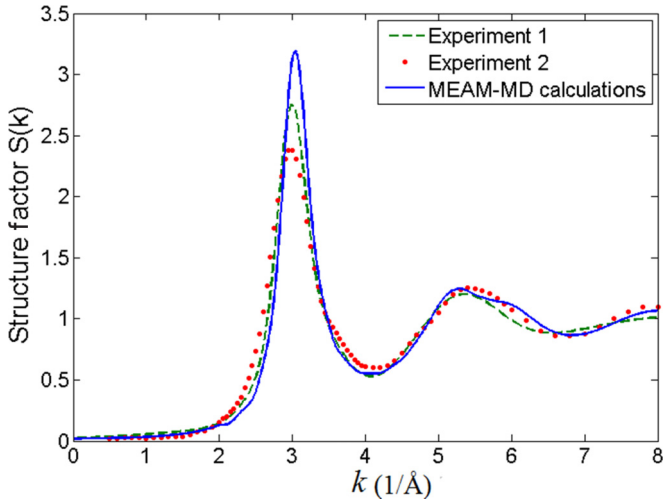
lated, which is depicted in Fig. 5 along with the experimental data. The calculated liquid structure factor matches reasonably well with the experiments with two exceptions. First, MEAM-MD simulations give a height of the first peak that is 16.8% and 34.0% higher than the experimental measurements in Refs. [55] and [56], respectively. Second, the MEAM-MD calculated liquid structure factor exhibits a splitting of the second peak similar to the EAM-MD calculations presented by Mendelev *et al.* [23].

F. Atom fluctuations

The mean-square displacement of atoms quantifies the fluctuation of atoms in the solid state, and it is necessary information to calculate PFC model parameters in the next section. In order to calculate the mean-square displacement of atoms in the solid state, a simulation box consisting of $10 \times 10 \times 10$ lattice cells is equilibrated for 0.5 ns at $T_M = 1807$ K with zero pressure in all directions. The time step size of 0.0005 ps is used for the MD simulations of this section. Then, a snapshot of the atoms' positions is taken every 0.01 ps for the simulation lasting up to 0.3 ns. The motion path of each atom (2000 atoms in total) is followed separately over time. The amplitude of the fluctuation in one direction is obtained as half of the difference between the two consecutive local maximum and minimum, which is averaged over the whole simulation time. The whole calculation is repeated for the movement of the atom in the two other directions, and the root-mean-square displacement of the atom i ($\sqrt{\langle |\boldsymbol{r}_i|^2 \rangle}$) is obtained. Finally, the whole calculation is repeated for all of the atoms, and the mean-square displacement of the atoms in the solid at 1807 K is calculated as $\sqrt{\langle |\boldsymbol{r}|^2 \rangle} = 0.3196$ Å.

III. PFC SIMULATIONS

In this section, we first briefly explain the one-mode PFC model and the adopted numerical procedure to solve PFC equations. Then, we relate the PFC parameters to the input

data from MD simulations and present an iterative procedure to determine these parameters. The PFC model is used to simulate solid-liquid equilibrating Fe by employing the developed parameters, and the results for the interface free energy, surface anisotropy, and expansion in melting are compared with the MEAM-MD results. Finally, to show an example of the application of this PFC model, the symmetric grain boundary free energy of Fe at the melting point is calculated for different misorientation angles.

A. PFC model and numerical procedure

The PFC model approximates the Helmholtz free energy (F) in the CDFT by expanding the ideal gas part and the correlation function in the Fourier space by fourth-order polynomials [2,16,17,57], resulting in

$$F = \int_V \left\{ \frac{1}{2} \phi(\mathbf{r}) \left[\alpha + \lambda \left(q_0^2 + \nabla^2 \right)^2 \right] \phi(\mathbf{r}) + \frac{g}{4} \phi(\mathbf{r})^4 \right\} d\mathbf{r}, \quad (9)$$

where $\phi(\mathbf{r})$ is a function related to the density field, and α, λ, q_0, and g are parameters to be determined for a specific material and temperature. Since this model includes only the first density wave in the formulation, it is called the one-mode PFC model. The dimensionless form of the PFC free energy is

$$F^* = \int_V \left\{ \frac{1}{2} \psi [-\varepsilon + (1 + \nabla^2)^2] \psi + \frac{\psi^4}{4} \right\} d\boldsymbol{x}, \quad (10)$$

where $\varepsilon = -\alpha/\lambda q_0^4$, $\psi = \phi \sqrt{g/\lambda q_0^4}$, $\boldsymbol{x} = q_0 \mathbf{r}$, and $F^* = (g/\lambda^2 q_0^5) F$. Since density is a conserved field, the time-evolution equation of the PFC model (ignoring the inertia term) is

$$\frac{\partial \psi}{\partial t^*} = \nabla^2 \frac{\delta F^*}{\delta \psi}, \quad (11)$$

where $t^* = t M \lambda q_0^3$, and M is the mobility constant. Assuming that ε is small, the PFC free energy is minimized by either a constant density for liquid, ψ_l, or a periodic density for solid, where the average density in the solid is $\bar{\psi}_s$. Therefore, the initial conditions for Eq. (11) for liquid is $\psi = \psi_l$ and for a solid with bcc configuration is

$$\psi = \bar{\psi}_s + 4A_s(\cos qx \, \cos qy + \cos qx \, \cos qz + \cos qy \, \cos qz). \quad (12)$$

Substituting Eq. (12) into Eq. (10), integrating over a lattice cell, and minimizing the resultant equation with respect to q and A_s lead to

$$A_s = -(2/15)\bar{\psi}_s + (1/15)\sqrt{5\varepsilon - 11\bar{\psi}_s^2}, \quad q = 1/\sqrt{2}. \quad (13)$$

For computational purposes, it is convenient to reduce the order of the spatial derivatives at Eq. (11) from six to two by introducing two new functions P and Q as

$$\frac{\partial \psi}{\partial t} = \nabla^2 [(1 - \varepsilon)\psi + 2P + Q + \psi^3],$$
$$P = \nabla^2 \psi, \quad Q = \nabla^2 P. \quad (14)$$

The system of PDEs in Eq. (14), with the initial conditions in Eq. (12) and periodic boundary conditions in all directions, is solved using the FEM, as implemented in COMSOL Multiphysics [58]. The implicit adaptive time stepping method along with the backward-Euler method are used for time discretization of the system of PDEs, and three-dimensional cubic elements are used for spatial discretization. For simulating the solid-liquid coexistence of Fe using the PFC model, we need to determine the model parameters α, λ, q_0, g, ψ_l, and $\bar{\psi}_s$, which will be addressed in the next section.

B. PFC parameter determination

In order to determine the PFC parameters, the density field is perturbed around the liquid density as $\psi = \psi_l + \delta\psi$, where $\delta\psi$ is the density perturbation, and the corresponding variation in the dimensional energy is calculated from Eq. (10) to be

$$\Delta F_{\text{PFC}} = \frac{\lambda q_0^4}{g} \int_V \frac{\delta\psi}{2}\big[\alpha + 3\lambda q_0^4 \psi_l^2 + \lambda\big(q_0^2 + \nabla^2\big)^2\big]\delta\psi\, d\boldsymbol{r}.$$
(15)

By assuming the correlation between only two particles, the corresponding CDFT free energy is

$$\Delta F_{\text{DFT}} = \frac{k_B T}{2} \int_V \int_{V'} d\boldsymbol{r}\, d\boldsymbol{r}'\, \delta\rho(\boldsymbol{r}')\left[\frac{\delta(\boldsymbol{r}-\boldsymbol{r}')}{\rho_0}\right.$$
$$\left. - C(|\boldsymbol{r}-\boldsymbol{r}'|)\right]\delta\rho(\boldsymbol{r}),$$
(16)

where

$$\delta\rho = \rho - \rho_l = \delta\phi = \sqrt{\lambda q_0^4/g}\,\delta\psi$$
(17)

and ρ_l is the reference liquid density. Applying Fourier transform to Eqs. (15) and (16) results in

$$\Delta F_{\text{PFC}} = \frac{\lambda q_0^4}{g} \int \frac{\delta\psi_k \delta\psi_{-k}\, d\boldsymbol{k}}{2}\big[\alpha + 3\lambda q_0^4 \psi_l^2 + \lambda\big(q_0^2 - k^2\big)^2\big],$$
$$\Delta F_{\text{DFT}} = \frac{k_B T}{\rho_l}\frac{\lambda q_0^4}{g} \int \frac{\delta\psi_k \delta\psi_{-k}\, d\boldsymbol{k}}{2}[1 - C(k)],$$
(18)

where $\delta\psi_k$ and $C(k)$ are the Fourier transforms of $\delta\psi$ and $\rho_l C(|\boldsymbol{r}|)$, respectively, and k is the Fourier space parameter. By equating ΔF_{PFC} and ΔF_{DFT} in Eq. (18), a relation between the liquid structure factor, $S(k) = 1/[1 - C(k)]$, and the PFC parameters will be attained

$$S(k) = \frac{k_B T}{\rho_l\big[\alpha + 3\lambda q_0^4 \psi_l^2 + \lambda\big(q_0^2 - k^2\big)^2\big]}.$$
(19)

The peak of the above expression taking place at $k = k_m = q_0$ is equal to

$$S(k_m) = \frac{k_B T}{\rho_l\big(\alpha + 3\lambda q_0^4 \psi_l^2\big)}.$$
(20)

The second relation in determining PFC parameters is obtained by finding the second derivative of $C(k)$ at the first peak of the structure factor, which is

$$C''(k_m) = \frac{S''(k_m)}{S^2(k_m)} = -\frac{8\lambda k_m^2 \rho_l}{k_B T}.$$
(21)

Utilizing the relation $\varepsilon = -\alpha/\lambda q_0^4$ and Eqs. (20) and (21), we obtain

$$\varepsilon = 3\psi_l^2 + \frac{8}{S(k_m)C''(k_m)k_m^2}.$$
(22)

Considering Eq. (12) for the solid density and comparing the real and dimensionless densities in Eq. (17), a relation for parameter g in terms of A_s and the solid-density wave amplitude (u_s) is obtained as

$$g = \frac{\lambda q_0^4 A_s^2}{\rho_l^2 u_s^2}.$$
(23)

Equations (20)–(23) determine the PFC parameters ε, λ, α, q_0, and g in terms of k_m, $S(k_m)$, $C''(k_m)$, u_s, ρ_l, ψ_l, and A_s. The parameters k_m, $S(k_m)$, and $C''(k_m)$ are obtained from the liquid structure factor curve calculated from the MD simulations in Sec. II E. Since metals are homogenous materials, the solid-density wave amplitude is related to the mean-square displacement by this relation: $u_s = \exp(-k_m^2 \langle|\boldsymbol{r}|^2\rangle/3)$ [59]. The mean-square displacement is calculated in Sec. II F using MD simulations. The parameter ρ_l is the liquid density at the melting point, which is also obtained from MD simulations.

For small ε, the dimensionless density field in the PFC model may be approximated by [18] $\psi = \psi_0 \varepsilon^{1/2}$; consequently, $\psi_l = \psi_{0l}\varepsilon^{1/2}$, $\bar{\psi}_s = \psi_{0s}\varepsilon^{1/2}$, and $A_s = A_{0s}\varepsilon^{1/2}$. By utilizing the common tangent line relations between solid and liquid free energies, we can obtain $\psi_{s0} = \psi_{l0} = -\sqrt{45/103}$ and $A_{s0} = 1/15 \times \sqrt{320/103}$. Therefore, the relations for PFC parameters reduce to the relations given in Refs. [18,19] as

$$\alpha = -\frac{103k_B T}{32\rho_l S(k_m)}, \quad \lambda = -\frac{k_B T\, C''(k_m)}{8\rho_l k_m^2},$$
$$g = \frac{2k_B T}{45\rho_l^3 u_s^2 S(k_m)}, \quad q_0 = k_m.$$
(24)

The relations to determine PFC parameters in Eq. (24) are called GL fitting, following the nomenclature used by Jaatinen *et al.* [19]. However, we use the relations in Eq. (24) as our initial guess of the parameter ε to construct the common tangent line between the liquid and solid free energies-average density curves. The coexisting average solid and liquid densities are obtained from the common tangent line, the liquid density is substituted into Eq. (22), and the new ε parameter is determined. The whole calculations are repeated iteratively until the calculated ε converges to its final value. Table VII lists all the parameters obtained from the MEAM-MD simulations and the PFC parameters obtained from the iterative procedure. We have used all of the input data from the MD simulations to find the PFC model parameters to test the MD-PFC fitting procedure presented in this paper. As mentioned in Sec. II E, the MEAM-MD calculations result in minor errors in some of these input properties. For instance, MEAM-MD calculations underpredict the height of the first peak, at least by 16.8%, compared to the experiments (see Sec. II E). Therefore, the use of experimental values for the properties listed in the left column of Table VII, when determining the PFC model parameters, is anticipated to improve the accuracy of the PFC calculations.

TABLE VII. Input parameters for PFC simulations obtained from MEAM-MD simulations along with the calculated PFC parameters using the iterative procedure.

MD parameters	Value	PFC parameters	Value
$q_0 = k_m$ (1/Å)	3.037	λ (eV Å^7)	0.2584
$S(k_m)$	3.191	α (eV Å^3)	-1.8022
$C''(k_m)$ (Å^2)	-9.50	g (eV Å^9)	9.2023
u_s	0.731	ψ_l	-0.1921
ρ_l (atom/Å^3)	0.0776	ψ_s	-0.1857
ρ_s (atom/Å^3)	0.0803	A_s	0.03650
T_M (K)	1807	ε	0.08205

C. Solid-liquid interface properties

In this section, we utilize PFC simulations to obtain the solid-liquid interface free energy, surface anisotropy parameters, and expansion in melting. It is interesting to compare the results of MD simulations and PFC simulations because the PFC model acts at a larger time scale. To calculate the solid-liquid interface free energy and surface anisotropy using the PFC model, three different equilibrating solid-liquid structure of Fe consisting of $m \times n \times l$ periodic lattice cells are constructed, where the normal directions are [001], [110], and [111]. The solid-liquid interface free energy in dimensional units for the solid-liquid interface area of Ω are calculated using [18]:

$$\gamma = \frac{\lambda^2 q_0^5}{g\Omega} \int \left\{ f - \left(f_s \frac{\psi - \psi_l}{\bar{\psi} - \psi_l} - f_l \frac{\psi - \bar{\psi}}{\bar{\psi} - \psi_l} \right) \right\} d\boldsymbol{r}, \quad (25)$$

where f_l is the liquid energy density and f_s is the average solid energy density. First, a convergence study is conducted to investigate the effect of the simulation box size and the element size on the calculated interface free energy. For instance, it is observed that the interface free energy converges for a box and mesh size of $2 \times 2 \times 147$ and $\pi/3$, respectively, where [001] is the normal direction. This simulation consisting of 3.5×10^6 degrees of freedom takes about 48 hours to complete on a desktop computer with a 3.10 GHz 8-core processor. The simulation time to calculate the same quantity using the MEAM-MD model includes running the LAMMPS script for about 6 hours using 192 CPU cores of a cluster computer having 2.7 GHz processors and performing postprocessing on the same desktop computer for about 48 hours. Generally, the PFC model integrates over the fluctuations of atoms in the MD model and therefore requires fewer atoms for the simulations; this characteristic of the PFC model enables simulations in diffusive time scales. However, the PFC model requires the discretization of the spatial domain to solve its PDEs numerically, which confines the size of the model.

Table VIII compares the solid-liquid interface free energies $\gamma_{001}, \gamma_{110}, \gamma_{111}$, surface anisotropy parameters δ_1 and δ_2 (defined in Eq. (5)), anisotropy parameter ε_4, and expansion in melting ΔV calculated by different methods. The anisotropy parameter $\varepsilon_4 = (\gamma_{001} - \gamma_{110})/(\gamma_{001} + \gamma_{110})$ is a parameter that is traditionally used to explain the anisotropy of the fourfold symmetry in the phase-field modeling [60,61]. In Table VIII, the MEAM-MD calculations are the MD calculations of

TABLE VIII. Comparison of solid-liquid interface properties calculated by MEAM-MD and different PFC simulations.

Quantity	MEAM-MD[a]	GL-PFC1[b]	GL-PFC2[c]	PFC[a]
γ_{001} (mJ/m^2)	177.9	160.5	207.1	198.5
γ_{110} (mJ/m^2)	174.0	156.8	201.7	193.8
γ_{111} (mJ/m^2)	171.8	152.0	194.8	184.6
δ_1 (%)	5.2	7.5	–	8.9
δ_2 (%)	-0.31	-0.94	–	-1.6
ε_4 (%)	1.10	1.15	1.3	1.20
ΔV (Å^3/Atom)	0.44	2.0[*]	2.07	1.36

[a]Present paper
[b]Reference [18]
[c]Reference [19]
[*]Calculated in this paper using the PFC parameters in Ref. [18].

the preceding section where the interface free energies for each normal to the interface direction are calculated as the average value from Eq. (5). The GL-PFC1 results refer to the PFC calculations of Wu and Karma [18], which differ in two ways from the current PFC calculations. The GL-PFC1 parameters were not calculated using the explained iterative procedure, and the MD input parameters are based on EAM-MD simulations of Sun *et al.* [24]. In addition, we have utilized the GL-PFC1 parameters to calculate the expansion in melting. The GL-PFC2 refers to the results presented by Jaatinen *et al.* [19], wherein the parameter g is obtained numerically using the common tangent line of the solid and liquid free energy densities.

From the data shown in Table VIII, a number of interesting conclusions can be drawn. First, all the methods show that $\gamma_{001} > \gamma_{110} > \gamma_{111}$, and our MEAM-MD and PFC calculations of the interface free energies are in a reasonable agreement with this trend. Our PFC calculations show that the average solid-liquid interface free energy is 192 (mJ/m^2), which is in good agreement with the MEAM-MD and GL-PFC2 calculations. Also, all three surface anisotropy parameters calculated by MEAM-MD and PFC methods are in good agreement with each other. Furthermore, both MD and PFC calculations show that the δ_1 anisotropy parameter must be positive and the δ_2 anisotropy parameter must be negative for Fe. The positive δ_1 and negative δ_2 result in the lowest interface stiffness for the [001] direction and then for the [110] direction. Since the interface stiffness is directly related to the amount of energy needed to alter the position of the interface, the preferred orientations during dendritic solidification are [001] and then [110], which are in agreement with the discussion by Haxhimali *et al.* [62] on orientation selection in dendritic evolution. Finally, the current PFC model significantly improves the prediction of the expansion in melting compared to other PFC simulations.

D. Grain boundary free energy

We presented an iterative procedure to determine PFC parameters from MEAM-MD calculations in the preceding sections. We showed that such a PFC model predicts the solid-liquid interface properties of Fe, in reasonable agreement with MD methods. Therefore, the developed PFC parameters can be used to simulate different problems related to the grain
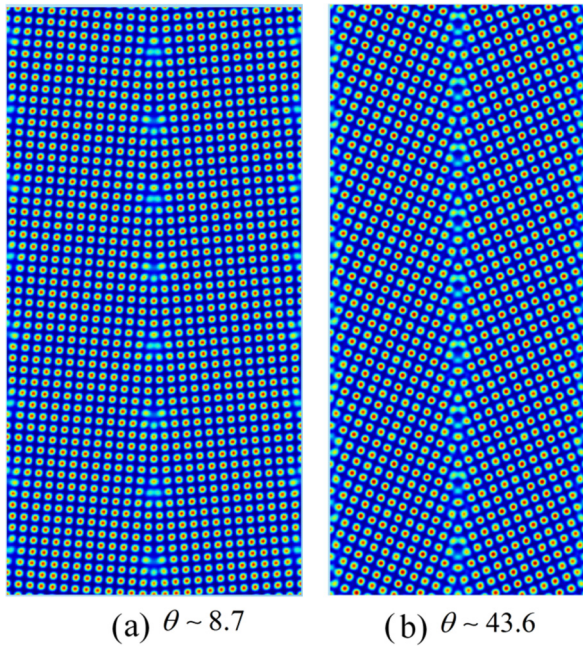
FIG. 6. (Color online) The PFC simulations of symmetric grain boundaries with misorientation angles: (a) $\theta \sim 8.7$ and (b) $\theta \sim 43.6$.

FIG. 7. (Color online) Plot of the grain boundary free energy γ_{GB} for Fe versus misorientation angle θ.

growth and evolution of Fe near the melting point. As an example of an application of this PFC model, the symmetric grain boundary free energy of Fe is determined in this section. The calculations are performed at the melting point using the parameters presented in Table VII. The normal to the plane of the grain boundary is the [001] direction, and the initial configuration consists of two periodic slabs oriented at $\theta/2$ and $-\theta/2$ with respect to the [100] axis to satisfy the periodic boundary conditions. This configuration results in two identical and parallel grain boundaries, where the interaction between them is negligible if a sufficient number of lattice cells are utilized along the normal direction to the grain boundary. The grain boundary free energy for the misorientation angle θ is calculated as half of the change in the free energy of the system after running the simulation for a long time. In this example, only mirror deformation with respect to the grain boundary plane is considered to determine the average value of the grain boundary free energy for a span of misorientation angles, i.e., small or large misorientation angles. For illustration purposes, the final configuration of the grain boundaries with misorientation angles of $\theta \sim 43.6$ and $\theta \sim 8.7$ are depicted in Figs. 6(a) and 6(b), respectively.

Figure 7 shows the variation of the grain boundary free energy γ_{GB} versus the misorientation angle calculated by PFC simulations. The general behavior of this curve is similar to what was obtained by Jaatinen *et al.* [19] using a PFC simulation. They showed that for small misorientation angles, this behavior is similar to the Read-Shockley [63] equation. Our calculations predict approximately 10% bigger γ_{GB} for all misorientation angles compared with those calculated by Jaatinen *et al.* [19] For instance, Jaatinen *et al.* calculated the γ_{GB} for large misorientation angles as $380\,(\text{mJ/m}^2)$ compared to our calculations of $\sim 420\,(\text{mJ/m}^2)$. The average grain boundary free energy of δ iron at 1673–1808 K was
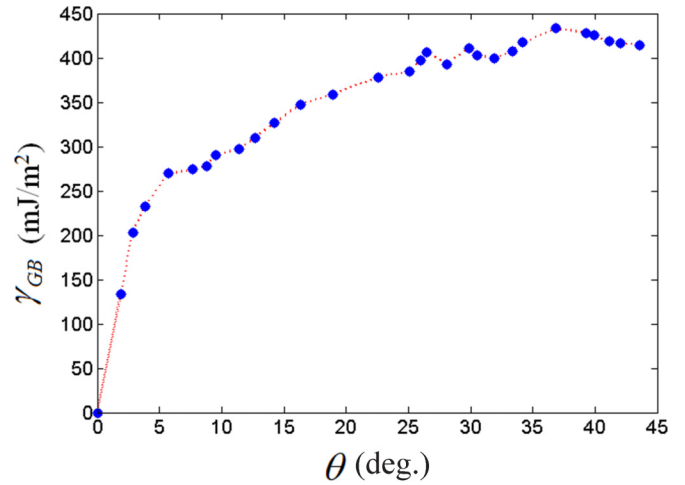
experimentally measured to be $470\,(\text{mJ/m}^2)$ [64]. Since the real material has more grain boundaries with large misorientation angles, it can be concluded that our calculations are in reasonable agreement with the experiments.

There is an interesting point to note regarding our PFC calculations of solid-liquid interface free energy and high-angle grain boundary free energy. The results reported in Table VIII indicate that the solid-liquid interface free energy of Fe for all the orientations is approximately in the range of 185–200 (mJ/m^2). Also, the average high-angle grain boundary free energy of Fe is $\sim 420\,(\text{mJ/m}^2)$. Therefore, the high-angle grain boundary free energy is bigger than twice the solid-liquid interface free energy of Fe at its melting point; thus, the grain boundary is completely wet [65,66]. From a microscopic point of view, this means that if a droplet of molten Fe is placed at the high-angle grain boundary of Fe, the droplet will spread into a uniform layer because the dihedral angle of the grain boundary in contact with the liquid is zero.

IV. CONCLUSIONS

A procedure to quantify a PFC model on diffusive time scales for simulating the solid-liquid interface of Fe was presented. The procedure was based on determining PFC parameters from MD simulations at the melting point. A 2NN MEAM parameter set for Fe was developed, which resulted in MD predictions to be very close to experimental measurements of the melting point (0.2% error), latent heat (5.8% error), and the expansion in melting (6.0% error), without a significant loss of accuracy in the prediction of low temperature properties, such as elastic constants, surface free energies, and vacancy formation energy. The MEAM-MD simulations were utilized to calculate the liquid structure factor and solid atoms fluctuation as input properties to determine the PFC model parameters. The one-mode PFC model was employed for simulations on diffusive time scales, and the PFC model parameters were determined by utilizing an iterative method. The governing PDEs were solved using the FEM.

The solid-liquid interface free energy for different interface planes and three surface anisotropy parameters were calculated

using MEAM-MD and PFC simulations. The results of MEAM-MD simulations were in good agreement with those of PFC simulations, validating the accuracy of the proposed iterative fitting procedure. To calculate the interface free energy and anisotropy using MD simulations, we defined an order parameter in the context of CFM to calculate these properties from MD simulations. This order parameter has less fluctuation at the solid and liquid, which makes the identification of the interface easier. The obtained average solid-liquid interface free energy was in good agreement with the result of EAM potential of Ackland *et al.* [52]. Also, the predictions of anisotropy parameter $\varepsilon_4 = (\gamma_{001} - \gamma_{110})/(\gamma_{001} + \gamma_{110})$ and the fourfold and sixfold symmetry anisotropy parameters by MEAM-MD simulations were in good agreement with the PFC predictions. In particular, we showed that both methods predict positive fourfold anisotropy and negative sixfold anisotropy, which result in growth preference primarily in the [001] direction and secondarily in the [110] direction during dendritic solidification.

Furthermore, it was shown that the present PFC model significantly improved the prediction of expansion in melting compared with other one-mode PFC models in the literature. The PFC model was also utilized to calculate the grain boundary free energy of Fe versus misorientation angle near the melting point. The PFC simulations predicted grain boundary free energies to be in agreement with the Read-Shockley equation for small misorientation angles and comparable to the experimental data for large misorientation angles.

[1] K. R. Elder, M. Katakowski, M. Haataja, and M. Grant, Phys. Rev. Lett. **88**, 245701 (2002).

[2] K. R. Elder and M. Grant, Phys. Rev. E **70**, 051605 (2004).

[3] H. Emmerich, H. Löwen, R. Wittkowski, T. Gruhn, G. I. Tóth, G. Tegze, and L. Gránásy, Adv. Phys. **61**, 665 (2012).

[4] H. Humadi, N. Ofori-Opoku, N. Provatas, and J. J. Hoyt, JOM **65**, 1103 (2013).

[5] S. van Teeffelen, R. Backofen, A. Voigt, and H. Löwen, Phys. Rev. E **79**, 051404 (2009).

[6] N. Pisutha-Arnond, V. W. L. Chan, K. R. Elder, and K. Thornton, Phys. Rev. B **87**, 014103 (2013).

[7] J. Berry, K. R. Elder, and M. Grant, Phys. Rev. B **77**, 224114 (2008).

[8] J. Mellenthin, A. Karma, and M. Plapp, Phys. Rev. B **78**, 184110 (2008).

[9] J. Berry, M. Grant, and K. R. Elder, Phys. Rev. E **73**, 031609 (2006).

[10] K. R. Elder, K. Thornton, and J. Hoyt, Philos. Mag. **91**, 151 (2011).

[11] M. Greenwood, N. Provatas, and J. Rottler, Phys. Rev. Lett. **105**, 045702 (2010).

[12] N. Ofori-Opoku, V. Fallah, M. Greenwood, S. Esmaeili, and N. Provatas, Phys. Rev. B **87**, 134105 (2013).

[13] J. Berry, N. Provatas, J. Rottler, and C. W. Sinclair, Phys. Rev. B **86**, 224112 (2012).

[14] E. Asadi and M. Asle Zaeem, JOM **67**, 186 (2015).

[15] K. R. Elder, N. Provatas, J. Berry, P. Stefanovic, and M. Grant, Phys. Rev. B **75**, 064107 (2007).

[16] S. Brazovskii, Soviet J. Exp. Theor. Phys. **41**, 85 (1975).

[17] J. Swift and P. Hohenberg, Phys. Rev. A **15**, 319 (1977).

[18] K.-A. Wu and A. Karma, Phys. Rev. B **76**, 184107 (2007).

[19] A. Jaatinen, C. V. Achim, K. R. Elder, and T. Ala-Nissila, Phys. Rev. E **80**, 031602 (2009).

[20] O. Kapikranian, H. Zapolsky, C. Domain, R. Patte, C. Pareige, B. Radiguet, and P. Pareige, Phys. Rev. B **89**, 014111 (2014).

[21]] G. Shen, M. L. Rivers, S. R. Sutton, N. Sata, V. B. Prakapenka, J. Oxley, and K. S. Suslick, Phys. Earth Planet. Inter. **143-144**, 481 (2004).

[22] F. J. Cherne, M. I. Baskes, and P. A. Deymier, Phys. Rev. B **65**, 024209 (2001).

[23] M. Mendelev, S. Han, D. Srolovitz, G. Ackland, D. Sun, and M. Asta, Philos. Mag. **83**, 3977 (2003).

[24] D. Y. Sun, M. Asta, and J. J. Hoyt, Phys. Rev. B **69**, 174103 (2004).

[25] Y. Watanabe, Y. Shibuta, and T. Suzuki, ISIJ International **50**, 1158 (2010).

[26] G. Ackland and M. Finnis, Philos. Mag. A **54**, 301 (1986).

[27] M. Finnis and J. Sinclair, Philos. Mag. A **50**, 45 (1984).

[28] J. Liu and H. Dong, in *IOP Conference Series: Materials Science and Engineering* (IOP Publishing, Schladming, Austria, 2012), p. 012113.

[29] J. Liu, R. Davidchack, and H. Dong, Comput. Mater. Sci. **74**, 92 (2013).

[30] G. Ackland, M. Mendelev, D. Srolovitz, S. Han, and A. Barashev, J. Phys.: Condens. Matter **16**, S2629 (2004).

[31] B. Jelinek, S. Groh, M. F. Horstemeyer, J. Houze, S. G. Kim, G. J. Wagner, A. Moitra, and M. I. Baskes, Phys. Rev. B **85**, 245102 (2012).

[32] E. Asadi, M. A. Zaeem, and M. I. Baskes, JOM **66**, 429 (2014).

[33] S. Plimpton, J. Comput. Phys. **117**, 1 (1995).

[34] M. I. Baskes, Phys. Rev. B **46**, 2727 (1992).

[35] S. Nouranian, M. A. Tschopp, S. R. Gwaltney, M. I. Baskes, and M. F. Horstemeyer, Phys. Chem. Chem. Phys. **16**, 6233 (2014).

[36] E. Asadi, M. A. Zaeem, A. Moitra, and M. A. Tschopp, J. Phys.: Condens. Matter **26**, 115404 (2014).

[37] B.-J. Lee and M. I. Baskes, Phys. Rev. B **62**, 8564 (2000).

[38] B.-J. Lee, W.-S. Ko, H.-K. Kim, and E.-H. Kim, Calphad **34**, 510 (2010).

[39] M. I. Baskes, J. S. Nelson, and A. F. Wright, Phys. Rev. B **40**, 6085 (1989).

[40] B.-J. Lee, M. I. Baskes, H. Kim, and Y. K. Cho, Phys. Rev. B **64**, 184102 (2001).

[41] J. H. Rose, J. R. Smith, F. Guinea, and J. Ferrante, Phys. Rev. B **29**, 2963 (1984).

[42] H. M. Ledbetter and R. P. Reed, J. Phys. Chem. Ref. Data **2**, 531 (1973).

[43] S. Nosé, J. Chem. Phys. **81**, 511 (1984).

[44] W. G. Hoover, Phys. Rev. A **31**, 1695 (1985).

[45] E. Asadi, M. Asle Zaeem, S. Nouranian, and M. I. Baskes, Acta Mater. **86**, 169 (2015).

[46] T. Lee, M. I. Baskes, S. M. Valone, and J. Doll, J. Phys.: Condens. Matter **24**, 225404 (2012).

[47] A. T. Dinsdale, Calphad **15**, 317 (1991).

[48] W. Fehlner and S. Vosko, Can. J. Phys. **54**, 2159 (1976).

[49] J. J. Hoyt, M. Asta, and A. Karma, Phys. Rev. Lett. **86**, 5530 (2001).

[50] R. L. Davidchack, J. R. Morris, and B. B. Laird, J. Chem. Phys. **125**, 094710 (2006).

[51] A. Karma, Phys. Rev. E **48**, 3441 (1993).

[52] G. Ackland, D. Bacon, A. Calder, and T. Harry, Philos. Mag. A **75**, 713 (1997).

[53] A. Carlsson, Solid State Phys. **43**, 1 (1990).

[54] E. Lorch, J. Phys. C **2**, 229 (1969).

[55] A. Il'inskii, S. Slyusarenko, O. Slukhovskii, I. Kaban, and W. Hoyer, Mater. Sci. Eng. A **325**, 98 (2002).

[56] Y. Waseda, *The Structure of Non-Crystalline Materials: Liquids and Amorphous Solids* (McGraw-Hill International Book Company, New York, 1980).

[57] K. R. Elder, M. Katakowski, M. Haataja, and M. Grant, Phys. Rev. Lett. **88**, 245701 (2002).

[58] COMSOL Multiphysics Users' Guide. COMSOL Inc. (2012).

[59] B. E. Warren, *X-ray Diffraction* (Courier Dover Publications, Mineola, NY, 1969).

[60] A. Karma and W.-J. Rappel, Phys. Rev. E **57**, 4323 (1998).

[61] N. Provatas, N. Goldenfeld, and J. Dantzig, Phys. Rev. Lett. **80**, 3308 (1998).

[62] T. Haxhimali, A. Karma, F. Gonzales, and M. Rappaz, Nat. Mater. **5**, 660 (2006).

[63] W. Read and W. Shockley, Phys. Rev. **78**, 275 (1950).

[64] A. Price, H. Holl, and A. Greenough, Acta Metall. **12**, 49 (1964).

[65] Y. Mishin, W. Boettinger, J. Warren, and G. McFadden, Acta Mater. **57**, 3771 (2009).

[66] M. Tang, W. C. Carter, and R. M. Cannon, Phys. Rev. B **73**, 024102 (2006).